Evidence and Model for Strain-Driven Release of Metal Nano-Catalysts from Perovskites during Exsolution

Tae-Sik Oh,† Ehsan K. Rahani,‡ Dragos Neagu,§ John T. S. Irvine,§ Vivek B. Shenoy,,‡ Raymond J. Gorte,† and John M. Vohs*,†*

†Department of Chemical and Biomolecular Engineering, University of Pennsylvania, 311A Towne Building, 220 S. 33rd Street, Philadelphia, Pennsylvania 19104, United States

‡Department of Materials Science and Engineering, University of Pennsylvania, 3231 Walnut Street, Philadelphia, Pennsylvania 19104, United States

§School of Chemistry, University of St. Andrews, Fife KY16 9ST, Scotland, United Kingdom

AUTHOR INFORMATION

Corresponding Author

*E-mail: vshenoy@seas.upenn.edu, *E-mail: vohs@seas.upenn.edu.

ABSTRACT. The evolution of the surface morphology during exsolution of Ni from the perovskite, $La_{0.4}Sr_{0.4}Ti_{0.97}Ni_{0.03}O_{3-\delta}$, under reducing conditions was determined using atomic force microscopy (AFM). The exsolution process was found to initially induce the formation of a 20-30 nm deep pit on the oxide surface followed by the emergence of a Ni particle at the bottom of the pit. Continued emergence of the particle results in it nearly filling the pit producing a unique structure in which the Ni particle is socketed into the oxide surface. We also show that this morphological evolution can be explained using a simple energy-based model that accounts for the interplay between the surface free energy and the strain energy induced by the included metal nucleate. The unique socketed structure results in strong anchorage between the exsolved particles and the oxide host lattice which imparts both high thermal stability and unique catalytic activity.

TOC GRAPHICS

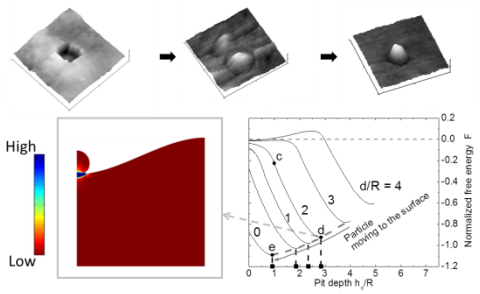

KEYWORDS. metal exsolution, perovskite, strain, atomic force microscopy

While supported metal catalysts are used extensively in the chemical process industries, maintaining high metal dispersion and avoiding deleterious reactions, such as coking (i.e. formation of a deleterious carbonaceous layer), often limits catalyst lifetime and effectiveness. Exsolution of metal nanoparticles from a host oxide lattice, which was first proposed by researchers at Daihatsu and Toyota,[1] has emerged as a promising synthesis method to overcome some of these limitations. In this approach metal cations dissolved in an oxide lattice, typically a perovskite, exsolve from the lattice under reducing conditions and condense into catalytically active metal nanoparticles which decorate the oxide surface. A striking feature of the exsolved metal nanoparticles is their exceptional coarsening and coking resistance while maintaining catalytic activity for desirable oxidation and reforming reactions.[2] These positive aspects are likely due to the exsolved nanoparticles forming a socketed or particle-in-a-pit structure with the oxide surface as has been revealed by transmission electron microscopy (TEM).[2–6] The work reported here provides the first combined experimental and theoretical study which elucidates the mechanism by which the exsolved particles become embedded into the oxide surface in the first place, rather than simply residing on its external surfaces or remaining inside the lattice. In particular, we have investigated the morphological evolution over the course of Ni particle exsolution from the A-site deficient perovskite, $La_{0.4}Sr_{0.4}Ti_{0.97}Ni_{0.03}O_{3-\delta}$, (Ni-doped LST). In addition to being a good model system, Ni-doped LST is representative of range of oxides that have been shown to be active for metal exsolution and suitable as the electrochemically active phase in electrodes in solid oxide electrochemical cells.[7–11]

The A-site deficiency in $La_{0.4}Sr_{0.4}Ti_{0.97}Ni_{0.03}O_{3-\delta}$ promotes exsolution of the more reducible Ni B-site cation[3] and it has previously been observed that the exsolved Ni forms the aforementioned particle-in-a-pit structure.[2,3] The exsolution process was imaged using atomic force microscopy

(AFM) whose sub-nanometer height resolution allows minute changes in the surface morphology, such as those that occur during the initial stages of the exsolution process, to be detected. Prior to reduction, sintered pellet samples were broken to obtain smooth fractured surfaces suitable for investigation. It is known that native surfaces can go through surface reconstruction that may hinder particle exsolution.[2] Varying the reduction temperature and duration with AFM images collected ex situ at various stages provided detailed insight into the exsolution process.

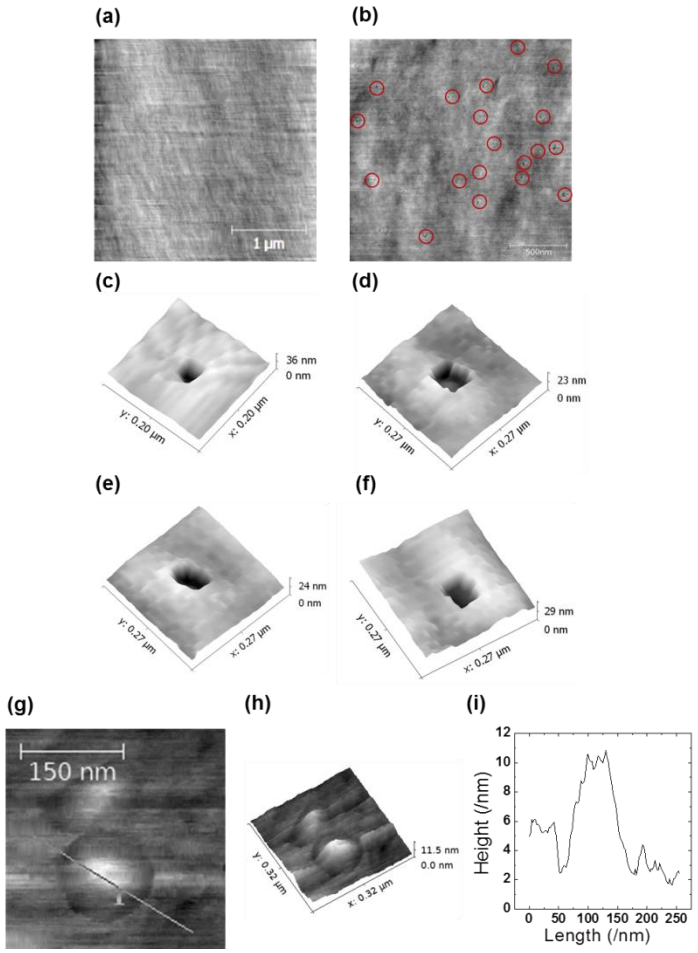

Figure 1. Initial pit formation and morphological evolution for nickel particle exsolution. (a) AFM image of as-fractured surface before reduction. There is no noticeable feature at this stage. (b) Multiple pits formed after reduction at 600 °C (15 min, dry H_2). (c), (d), (e), (f) 3D images of four different pits formed after reduction at 600 °C (45 min, dry H_2). All four pits were found in one scan area (2µm × 2 µm). (g) AFM image after reduction at 700 °C (15 min, dry H_2). (h) 3D view of (g). (i) AFM height profile along the line shown in (g).

Figure 1a displays an AFM image of the fractured Ni-doped LST surface prior to reduction. This image shows that the surface is relatively smooth with a root-mean-square roughness of 1.2 nm. Secondary electron microscopy images of non-fractured surfaces (not shown), showed that the individual grains were larger than 10 μm in diameter, so the AFM images are effectively sampling a single grain. Initial reduction induces the formation of multiple small indentations or pits on the oxide surface (Figure 1b). Figures 1c-f show close up 3-dimensional images of several pits that formed upon mild reduction in dry H2 at 600 °C for 45 min. Note that for the sintering conditions used to produce this sample (1500 °C, 4h) it is unlikely that these features could be due to interior pores exposed upon fracture. AFM images of further morphological evolution upon additional reduction at 700 °C, Figures 1g and 1h, show the emergence of a metal particle in the center of each pit, resulting in a partially submerged particle surrounded by a trench (see line scan in Figure 1i). These results suggest that Ni particle nucleation takes place underneath the surface followed by emergence of the particle through the surface. Metal particle nucleation within the oxide matrix has been reported,[12] but often not in the context of catalytic applications.[13] If Ni atoms emerging randomly onto the surface, followed by surface diffusion were the only possible mechanism to nucleate particles, this observed morphologic evolution would not be expected. Indeed, as we have shown previously,[2] Ni particles produced by vapor deposition of Ni onto a Ni-doped LST do not form this structure and have different thermal stabilities and reactivities.

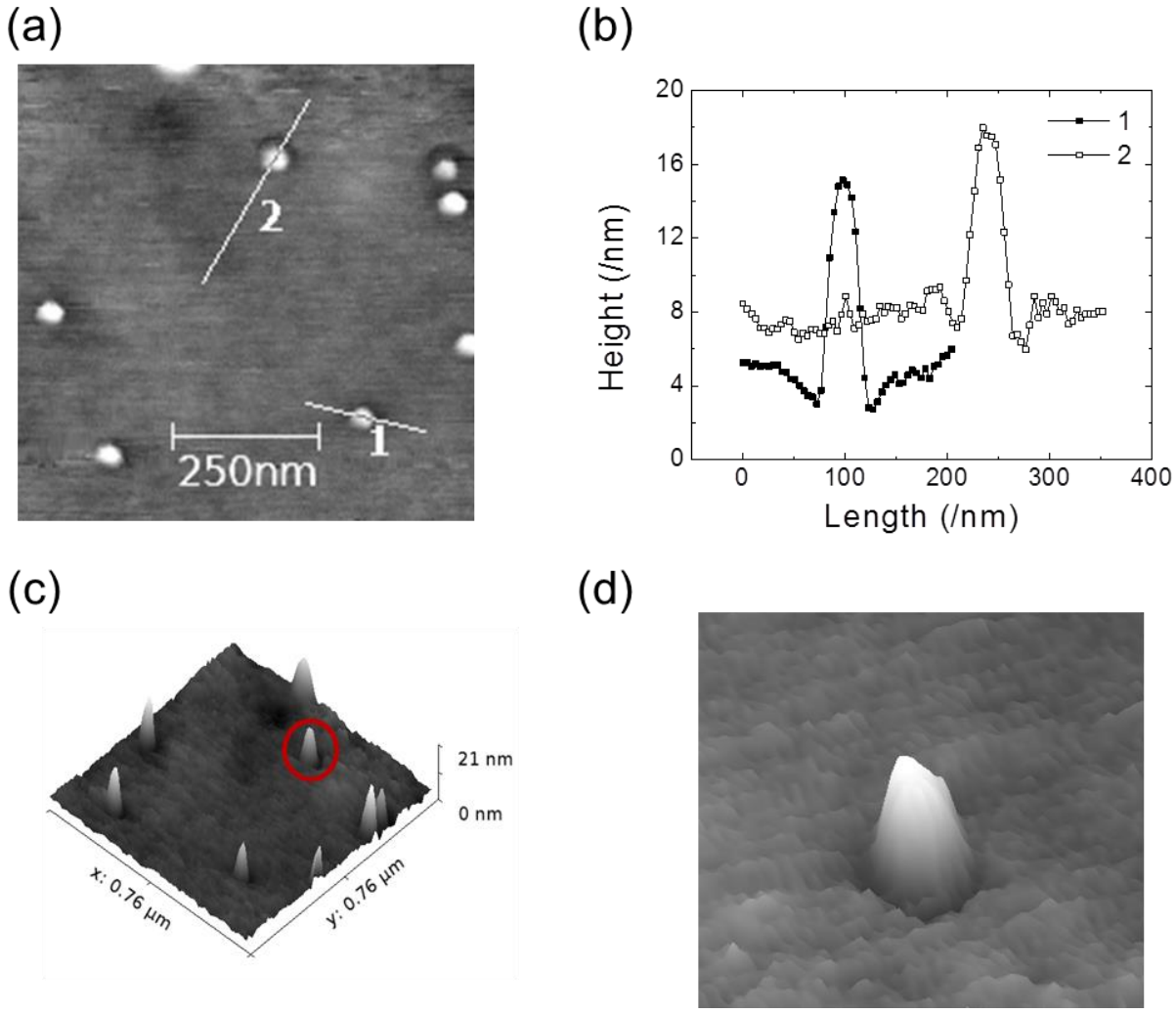

Figure 2. Intermediate stage of the Ni exsolution process. (a) AFM image of a fractured surface after reduction at 900 °C (15 min, dry H_2). (b) AFM height profiles along the lines in (a). Profile 2 is vertically shifted to higher z value for clarity. (c) 3D view of (a). (d) Magnified 3D view of a particle marked in (c). The height of this particle is estimated to be 11 nm from profile 2 in (b).

With additional reduction at 900 °C, the shape of the particle and surrounding trench becomes better defined compared to the earlier state as shown in Figure 2. Note that the trench depth is ~2 nm and the height of the exposed part of metal particle increases as exsolution proceeds. This agrees well with the proposed scenario where preformed nickel particles emerge from the sub-

surface region. Atomic Ni still possibly diffuses and attaches itself for particle growth during the outward movement of the particle though the extent of this contribution is difficult to quantify.

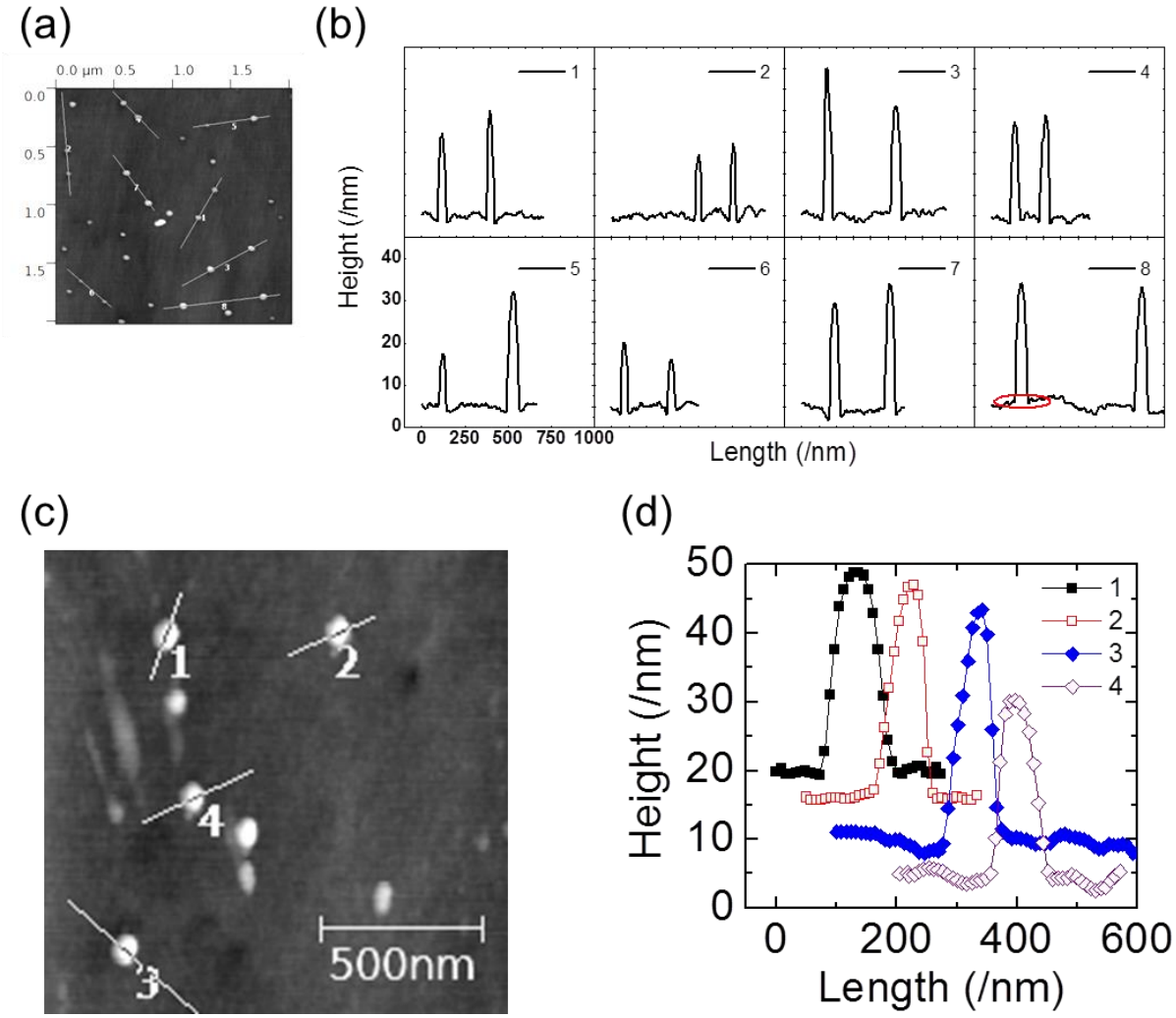

Figure 3. Morphology evolution during further exsolution. (a) AFM image of a fractured surface after reduction at 900 °C (5 h, dry H_2). (b) AFM height profiles along the lines in (a). All profiles are plotted in same scale. (c) AFM image of a fractured surface after reduction at 900 °C (30 h, dry H_2). (d) AFM height profiles along the lines in (c). Profiles are moved away from each other for clarity. Trenches around Ni exsolution particles becomes less obvious compared to (b).

Figure 3 shows AFM images and line scans obtained after prolonged reduction in H_2 at 900 °C. Additional growth/emergence of the Ni particles is observed, with particles as tall as 35 nm being produced. At this stage, the trenches around the particles become less pronounced as

marked with an oval on profile 8 in Figure 3b. The trench disappearance seemingly occurs when a substantial portion of the metal particle has escaped out of the lattice, although a trench is still present for a majority of the particles. With further aging for 30 h, it becomes harder to clearly identify trenches (Figure 3c-d) while the particle height does not show a significant increase.

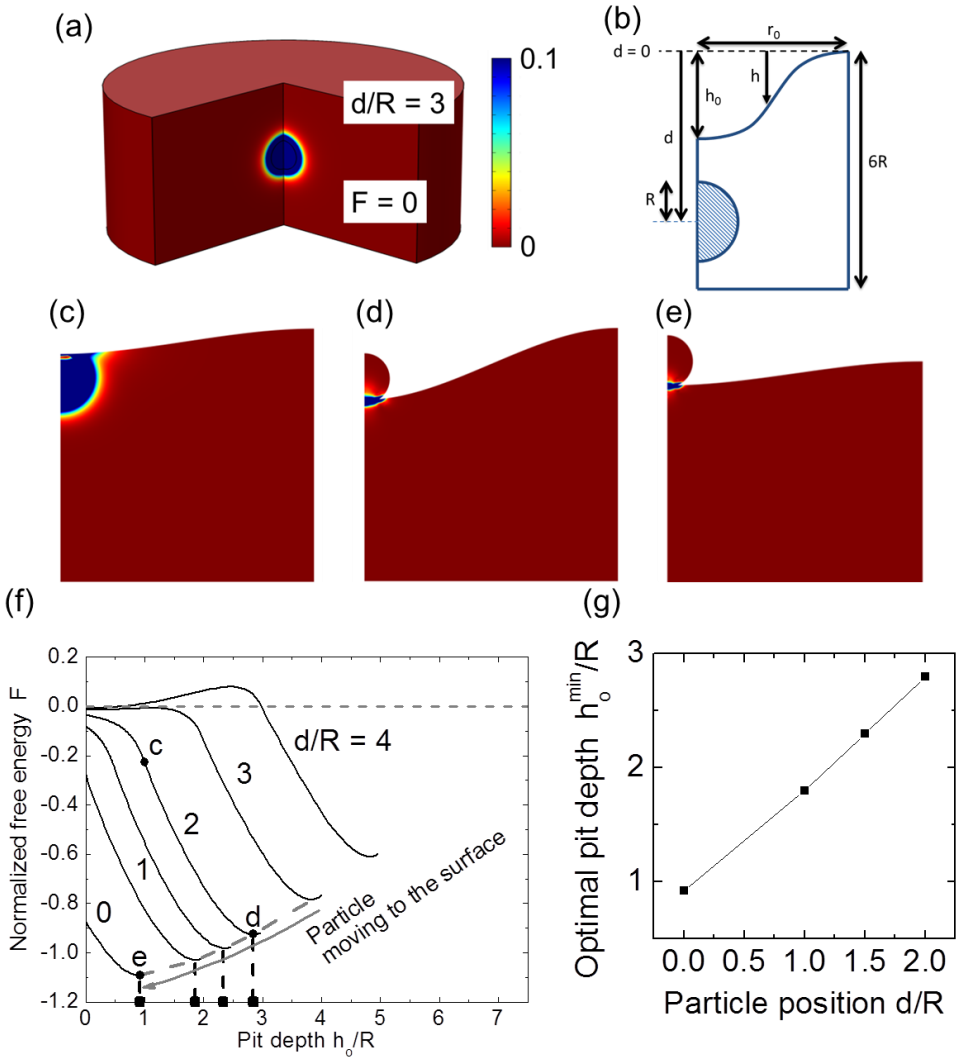

Figure 4. Strain field simulation results. (a) Reference state (F = 0) where Ni particle is in the middle of the matrix without energy relaxation. Color code denotes distribution of volumetric free energy density. (b) An axisymmetric model geometry. (c), (d), (e) Time-lapse spatial free energy density distributions as the system evolves to minimize F. (f) Calculated normalized free energy F versus pit depth. Corresponding particle position d/R values are marked on each line. Points c, d, and e matches the energy maps (c), (d), and (e). Each line has optimal pit depth as marked with black squares on x axis. Note the energy barrier for a particle located deep into bulk (d/R = 4). (g) Linear relation between the particle position and optimal pit depth h_0^{min}. 4 values from (f) are shown here.

Strain field modeling was used to gain mechanistic insight into the exsolution process and the origin of the unique particle-surface interface. As a starting point, we consider the interaction between a spherical metal nucleus already formed in the bulk, as shown in Figure 4a, and the surrounding oxide matrix. This particle will deform the surrounding oxide and induce an elastic strain in the system.

From an energetic point of view, if the particle can escape from the matrix and remain attached to the surface, the elastic energy can decrease since the surface of the particle is no longer constrained. This, on the other hand will lead to an increase in the surface energy, but if the particle is of sufficient size the elastic energy, which scales with the volume of the particle, may dominate over the surface energy, which scales with the area. As we will show below, the formation of pits provides a mechanism for the embedded particle to escape to the surface.

Deformation (pit formation) of the surface was approximated by a simple, idealized cubic function (see Figure 4b):

$$h(r) = 2h_O(\frac{r}{r_O})^3 - 3h_O(\frac{r}{r_O})^2 + h_O. \quad (1)$$

With this surface profile, the inflexion point is always at $r = r_o/2$, there is an extremum at $r = 0$, and the depth vanishes at $r = r_0$, and hence contains all the salient features observed in our experiments. Recent experiments show that the interface between the exsolved particle and the host lattice remains coherent,[3] suggesting that the difference in lattice constants will lead to straining of the particle. To capture this effect, a 10% mismatch strain is introduced to the nucleus ($\varepsilon_o = 0.1$) to account for lattice parameter difference between the metal inclusion and oxide matrix.

We find that as the nucleus approaches the surface, the surface profile evolves to form a recessed region lowering the total elastic strain energy; note that if the particle is closer to the

"free" surface, elastic energy can be relaxed more efficiently. This strain energy relaxation process inevitably involves increases in the surface energy of the pit, since the surface area increases by ΔA ($h_O > 0$). This competition can be explored by considering the total free energy of the system that can be written as follows:

$$F = \frac{\frac{1}{2}\int_{V_S} \sigma_{ij}\epsilon_{ij} dV + \gamma A_{nuc} + \gamma \Delta A - E_{ref}}{M V_{nuc} {\varepsilon_0}^2}, \quad (2)$$

where V_s is the volume of the simulation cell, and F is normalized by strain energy of the spherical nucleus with volume $V_{nuc} = \frac{4\pi R^3}{3}$ embedded deep in the matrix, which we call the "pre-relaxation" strain energy. The surface energy, γ, of the oxide matrix is assumed to be 1.41 J m^{-2} which was obtained by averaging the surface energies of SrO and TiO_2 terminations of the (100) plane.[14] In this first approximation model, the surface energy of the metal-gas interface is taken to be the same as the oxide-gas interface for simplicity so that $\gamma\Delta A$ accounts for the total surface free energy change regardless of involved phases. Since nickel-metal oxide interface energies reported in the literature tend to be between 1.5 and 2.1 J m^{-2}, [15,16] for simplicity we also used the 1.41 J m^{-2} value for the solid-solid interface energy around the nucleus (surface area = $A_{nuc.}$). E_{ref} was introduced to make F zero when the nucleus is at the center of the simulation cell (see Figure 4a). The bulk modulus and Poisson's ratios of the oxide and nucleus are assumed to be E_O = 284.3 GPa, $\nu_O = 0.22$,[17] and E_N = 207 GPa, $\nu_N = 0.31$,[18] respectively. The biaxial modulus is given by M =$E_N/(1-\nu_N)$.[19]

The elastic fields and the free energy were calculated via the Finite Element Method using the COMSOL Multiphysics package (version 4.3b). The computational domain (Figure 4b) was refined to 5231 triangular elements with the 2D axisymmetric formulation. The particle size, R, in Figure 4b is assumed to be 9 nm with $r_o = 10R$. The aim of our simulations was to obtain the

optimum pit depth (h_0^{min}) at which the non-dimensional free energy, *F,* attains a global minimum in its magnitude. A set of nuclei depths from the surface, *d/R*, were tested to see how the energy landscape varies with morphology.

A summary of the simulation results are presented in Figure 4f which plots the overall free energy as a function of the normalized pit depth for a series of *d/R* values. Each line corresponds to a constant value of d/R and shows the evolution of the free energy as the oxide surface is allowed to deform inwards. These simulations show that for $d/R < 3$ as the pit depth increases causing the metal particle to get closer to the surface, the free energy decreases until a minimum is obtained. This minimum occurs at the optimal pit depth, h_0^{min}. The initial decrease in free energy with increasing pit depth provides the driving force for deformation of the surface and pit formation. A calculation of the number of exsolvable Ni ions in the near surface region where $d/R < 3$ is sufficient to account for the particle/pit density and particle/pit sizes observed experimentally by AFM (see calculations in Supporting Information). In contrast, for metal particles embedded more deeply below the surface where $d/R \geq 3$, inward deformation of the surface initially causes the free energy to increase, resulting in an energy barrier to pit formation which increases with particle depth. This energy barrier prevents pit formation for these deeply embedded nuclei.

The spatial distribution of the elastic strain energy for $d/R = 2$ and several $\frac{h_0}{R}$ values are depicted in Figures 4c and 4d. The strain energy values in these figures have been normalized by the pre-relaxation energy density, $M{\varepsilon_0}^2$, and the scale for the dimensionless energy values is shown in Figure 4a. Figure 4c illustrates the moment when the nucleus touches the deformed oxide surface (this point is also denoted in Figure 4f). Note that there is little strain energy at the nucleus-surface contact point, whereas higher strain energy is present in the bulk of the nucleus.

Upon further surface deformation resulting in energy relaxation to the minimum value, the nuclei partially emerges through the oxide surface giving rise to the embedded particle-in-a-pit structure shown in Figure 4d. For this scenario the strain energy is localized at the particle-surface contact point as shown in the figure.

The energy landscape in Figure 4f also shows that the minimum free energy of the system and the optimal pit depth both decrease as d/R goes to zero. The strain energy distribution for $d/R = 0$ at the optimal pit depth is shown in Figure 4e. The net effect of this variation in free energy with decreasing d/R is to provide a driving force for pulling the particle through the surface. The pit depth for minimum free energy as a function of the particle position is plotted in Figure 4g. Together these two plots predict that the pit depth will decrease in the latter stages of particle exsolution which is in accordance with the experimental data in Figure 3.

In summary, in this work we have shown that (1) exsolution of metals from perovskites proceeds at least in part via formation of sub-surface nucleates, (2) movement of the metal nucleate towards the surface is accompanied by the formation of a pit on the surface from which the particle emerges, (3) the pit depth (or trench depth surrounding the particle) progressively decreases as the volume of the exposed particle increases, and (4) quantitative strain field modeling shows that the interplay between surface free energy and strain energy provides the driving force for exsolution and explains the observed morphology evolution and final particle-in-a-pit morphology that is responsible for the unique thermal stability and catalytic properties of supported metal nanoparticles formed in this manner.

Experimental Section

Sample Preparation: $La_{0.4}Sr_{0.4}Ti_{0.97}Ni_{0.03}O_{3-\delta}$ powders were made by sol-gel process. Stoichiometric amounts of $La(NO_3)_3 \cdot 6H_2O$ (Alfa Aesar), $Sr(NO_3)_2$ (Alfa Aesar), and $Ni(NO_3)_2 \cdot 6H_2O$ (Alfa Aesar) were used for A-site cation source and B-site dopant source. Titanium isopropoxide (Aldrich), citric acid (Fisher Scientific) and ethylene glycol (Fisher Scientific) were added in 0.97:4:16 molar ratio. Gelation occurred by heating, and resulting powder was calcined in air at 700 °C for 4 h to form perovskite phase, as confirmed by X-ray diffraction. Dry pressed pellets were sintered in air at 1500 °C for 4 h. All samples analyzed in present work are from single batch of powder.

Sample Reduction: Sintered pellets were fractured into multiple pieces to produce surfaces ready for reduction. Dry H_2, directly from gas tank, served as the reducing agent. Reducing gas flow started at room temperature and stopped only after the sample cools down to room temperature again. Reduction temperature ranges from 600 °C to 900 °C, and reduction time (dwell time at the preset reduction temperature) ranges from 15 minutes to 30 hours.

Atomic Force Microscopy (AFM): All images were collected in tapping mode using a Pacific Nanotechnology Nano-E microscope with commercially available silicon tips (NanoScience Instruments, Aspire CT300R) on fractured surface rather than native surface. Native surfaces are avoided to minimize effects from possible surface enrichment during high temperature sintering. All AFM image analyses were done in Gwyddion software package. Leveling was done with 2nd order polynomials in both directions in all cases. No efforts have been made to image a single specific region multiple times over the course of reduction.

ASSOCIATED CONTENT

Supporting Information. The following files are available free of charge.

Calculations of expected pit volumes and exsolved metal particle sizes. (PDF)

AUTHOR INFORMATION

Corresponding Author

*E-mail: vshenoy@seas.upenn.edu, *E-mail: vohs@seas.upenn.edu.

Notes

The authors declare no competing financial interests.

ACKNOWLEDGMENT

We thank the U.S. National Science Foundation (NSF) and the European Engineering and Physical Sciences Research Council for funding through the Materials World Network Program (grant nos. DMR-1210388 and EP/J018414/1). We also thank the NSF MRSEC Center at the University of Pennsylvania (DMR11-20901) for partial support of this work. VBS also acknowledges NSF support through grant CMMI-1363203.

REFERENCES

(1) Nishihata, Y.; Mizuki, J.; Akao, T.; Tanaka, H.; Uenishi, M.; Kimura, M.; Okamoto, T.; Hamada, N. Self-regeneration of a Pd-perovskite Catalyst for Automotive Emissions Control. *Nature* **2002**, *418*, 164–167.

(2) Neagu, D.; Oh, T.-S.; Miller, D. N.; Ménard, H.; Bukhari, S. M.; Gamble, S. R.; Gorte, R. J.; Vohs, J. M.; Irvine, J. T. S. Nano-socketed Nickel Particles with Enhanced Coking Resistance Grown in situ by redox exsolution. *Nat. Commun.* **2015**, *6*:8120.

(3) Neagu, D.; Tsekouras, G.; Miller, D. N.; Ménard, H.; Irvine, J. T. S. In Situ Growth of Nanoparticles through Control of Non-stoichiometry. *Nat. Chem*. **2013**, *5*, 916–923.

(4) Jardiel, T.; Caldes, M.T.; Moser, F.; Hamon, J.; Gauthier, G.; Joubert, O. New SOFC Electrode Materials: The Ni-substituted LSCM-based Compounds $(La_{0.75}Sr_{0.25})(Cr_{0.5}Mn_{0.5-X}Ni_X)O_{3-\delta}$ and $(La_{0.75}Sr_{0.25})(Cr_{0.5-X}Ni_XMn_{0.5})O_{3-\delta}$. *Solid State Ionics* **2010**, *181*, 894–901.

(5) Kobsiriphat, W.; Madsen, B.D.; Wang, Y.; Marks, L. D.; Barnett, S. A. $La_{0.8}Sr_{0.2}Cr_{1-X}Ru_XO_{3-\delta}$-$Gd_{0.1}Ce_{0.9}O_{1.95}$ Solid Oxide Fuel Cell Anodes: Ru Precipitation and Electrochemical Performance. *Solid State Ionics* **2009**, *180*, 257–264.

(6) Kobsiriphat, W.; Madsen, B.D.; Wang, Y.; Shah, M.; Marks, L. D.; Barnett, S. A. Nickel- and Ruthenium-Doped Lanthanum Chromite Anodes: Effects of Nanoscale Metal Precipitation on Solid Oxide Fuel Cell Performance. *J. Electrochem. Soc.* **2010**, *157*, B279–B284.

(7) Park, B. H.; Choi, G. M. Ex-solution of Ni Nanoparticles in a $La_{0.2}Sr_{0.8}Ti_{1-X}Ni_XO_{3-\delta}$ Alternative Anode for Solid Oxide Fuel Cell. *Solid State Ionics* **2014**, *262*, 343–348.

(8) Shin, T. H.; Okamoto, Y.; Ida, S.; Ishihara, T. Self-Recovery of Pd Nanoparticles That Were Dispersed over La(Sr)Fe(Mn)O_3 for Intelligent Oxide Anodes of Solid-Oxide Fuel Cells. *Chem. Eur. J.* **2012**, *18*, 11695–11702.

(9) Oh, T.-S.; Yu, A. S.; Adijanto, L.; Gorte, R. J.; Vohs, J. M. Infiltrated Lanthanum Strontium Chromite Anodes for Solid Oxide Fuel Cells: Structural and Catalytic Aspects. *J. Power Sources* **2014**, *262*, 207–212.

(10) Li, S.; Qin, Q.; Xie, K.; Wang, Y.; Wu, Y. High-performance Fuel Electrodes Based on $NbTi_{0.5}M_{0.5}O_4$ (M = Ni, Cu) with Reversible Exsolution of the Nano-catalyst for Steam Electrolysis. *J. Mater. Chem. A* **2013**, *1*, 8984–8993.

(11) Yang, C.; Yang, Z.; Jin, C.; Xiao, G.; Chen, F.; Han, M. Sulfur-Tolerant Redox-Reversible Anode Material for Direct Hydrocarbon Solid Oxide Fuel Cells. *Adv. Mater.* **2012**, *24*, 1439–1443.

(12) Katz, M. B.; Zhang, S.; Duan, Y.; Wang, H.; Fang, M.; Zhang, K.; Li, B.; Graham, G. W.; Pan, X. Reversible Precipitation/dissolution of Precious-metal Clusters in Perovskite-based Catalyst Materials: Bulk versus Surface Re-dispersion. *J. Catal.* **2012**, *293*, 145–148.

(13) Backhaus-Ricoult, M. Growth and Equilibrium Morphology of Metal Precipitates Formed Inside an Oxide Matrix. *Interface Science* **1997**, *4*, 285–302.

(14) Sano, T.; Saylor, D. M.; Rohrer, G. S. Surface Energy Anisotropy of $SrTiO_3$ at 1400°C in Air. *J. Amer. Ceram. Soc.* **2003**, *86*, 1933–1939.

(15) Nahor, H.; Meltzman, H.; Kaplan, W. D. Ni–YSZ(111) Solid–solid Interfacial Energy. *J. Mater. Sci*. **2014**, *49*, 3943–3950.

(16) Murr, L. E. Measurement of Interfacial Energy and Energy of Adhesion by Scanning Electron Microscopy. *Mater. Sci. Eng.*, **1973**, *12*, 277–283.

(17) Webb, S.; Jackson, I.; Gerald, J. F. Viscoelasticity of the Titanate Perovskites $CaTiO_3$ and $SrTiO_3$ at High Temperature. *Phys. Earth Planet Inter.* **1999**, *115*, 259–291.

(18) Ledbetter, H. M.; Reed, R. P. Elastic Properties of Metals and Alloys, I. Iron, Nickel, and Iron-Nickel Alloys. *J. Phys. Chem. Ref. Data* **1973**, *2*, 531–618.

(19) Tambe, D. T.; Shenoy, V. B. On the Energetic Origin of Self-limiting Trenches Formed around Ge/Si Quantum Dots. *Appl. Phys. Lett*. **2004**, *85*, 1586–1588.